Direct Numerical Simulations of Rayleigh-Taylor instability

D. Livescu, T. Wei and M. R. Petersen

Los Alamos National Laboratory, Los Alamos, NM 87545, USA

E-mail: `livescu@lanl.gov`

Abstract. The development of the Rayleigh-Taylor mixing layer is studied using data from an extensive new set of Direct Numerical Simulations (DNS), performed on the 0.5 Petaflops, 150k compute cores BG/L Dawn supercomputer at Lawrence Livermore National Laboratory. This includes a suite of simulations with grid size of $1024^2 \times 4608$ and Atwood number ranging from 0.04 to 0.9, in order to examine small departures from the Boussinesq approximation as well as large Atwood number effects, and a high resolution simulation of grid size $4096^2 \times 4032$ and Atwood number of 0.75. After the layer width had developed substantially, additional branched simulations have been run under reversed and zero gravity conditions. While the bulk of the results will be published elsewhere, here we present preliminary results on: 1) the long-standing open question regarding the discrepancy between the numerically and experimentally measured mixing layer growth rates and 2) mixing characteristics.

1. Introduction

Rayleigh-Taylor instability (RTI), which is generated at the interface between a heavy and light fluid, subjected to a constant gravitational field in an unstable configuration, is of fundamental importance in a multitude of applications ranging from fluidized beds, oceans and atmosphere, to inertial, magnetic, or gravitational confinement fusion, and to astrophysics [1, 2]. Although this instability has been subjected to intense research over the last 50 years, until recently, numerical studies have been restricted to coarse mesh calculations. On the other hand, it is notoriously difficult, in laboratory experiments, to accurately characterize and control the initial conditions and provide the detailed measurements needed for turbulence model development and validation. Thus, a large number of open questions remain unanswered about this instability and even first order global quantities, such as the layer growth, are not completely understood and still give rise to intense debate [3, 4]. Nevertheless, today's petascale computers allow fully resolved simulations of RTI at parameter ranges comparable to those attained in laboratory experiments, but providing, in carefully controlled initial and boundary conditions studies, much more information than the physical experiments. These extremely high resolution simulations are enabling a look at the physics of turbulence and turbulent mixing in unprecedented detail, hopefully contributing to a significant advance in our understanding of these phenomena.

The primary non-dimensional parameter characterizing differential acceleration effects is the Atwood number, $A = \frac{\rho_2 - \rho_1}{\rho_2 + \rho_1}$, where ρ_1, ρ_2 are densities of the light and heavy fluids, respectively. The Atwood number ranges from 0 to 1. For air inter-penetrating helium, for which the density ratio is $\frac{\rho_2}{\rho_1} \approx 7$, the Atwood number is $A \approx 0.75$. For air and hydrogen, $A = 0.85$. Similar Atwood numbers occur for mixing between liquid hydrocarbons and air. In contrast, the Boussinesq

approximation corresponds to $A \to 0$ and a value of 0.05 is usually taken to define this limit. Most previous numerical studies address the low to moderate A case (e.g. [5, 6, 1, 2, 3]) and no Direct Numerical Simulations have been published for $A > 0.5$. Yet, the development of the instability and the mixing itself are fundamentally different at high and low A [3]. For example, our previous results in an idealized triply-periodic buoyancy driven flow show that the mixing is asymmetric at large density ratios, with the pure light and heavy fluids mixing at different rates [7, 8]. At high A, due to the tight coupling between the density and velocity fields, even when the two fluids are incompressible, new cubic nonlinearities arise in addition to the quadratic non-linearities of the incompressible Navier-Stokes equations. Moreover, the velocity field is no longer solenoidal and the specific volume, a function of the amount of each material present, is a new dependent variable. We refer to such flows as variable-density (VD) flows.

In this paper we present preliminary results from an extensive new set of very high resolution Direct Numerical Simulations of Rayleigh-Taylor instability, covering the range of Atwood number from 0.04 to 0.9. In particular, one of the simulations, at $A = 0.75$ and grid size $4096^2 \times 4032$, is the largest fully resolved instability simulation performed to date. Some results concerning the base case $A = 0.04$ simulation have been discussed in Ref. [3] and preliminary results from some of the simulations have been presented in Ref. [9]. Nevertheless, the simulations are still being analyzed and the final results will be published elsewhere.

The paper is organized as follows. Section 2 presents the governing equations and numerical approach. Results concerning the instability growth and mixing characteristics across the Rayleigh-Taylor (RT) layer are discussed in section 3. A summary and concluding remarks are provided in section 4.

2. Governing equations and numerical methodology

The RTI simulations presented address the case of miscible incompressible materials. Thus, the two pure fluids have constant, but different, microscopic densities. In this case, the specific volume and density of the mixture are related to the microscopic densities, ρ_l, and mass fractions, Y_l, $l = \overline{1,2}$, of the two pure fluids by the relation

$$v = \frac{1}{\rho} = \frac{Y_1}{\rho_1} + \frac{Y_2}{\rho_2} \tag{1}$$

which simply states that the total mass inside of a control volume is the sum of the masses of the two fluids. Here $Y_1 + Y_2 = 1$ and the index "2" refers to the heavier fluid.

The resulting flow due to the instability development can be described by continuity and momentum transport equations. For binary mixtures with Fickian diffusion, the species mass fraction transport equations and relation 1 lead to a formula for the velocity divergence in terms of the derivatives of the density field. In non-dimensional form, these equations are [3, 7, 5, 10]:

$$\frac{\partial}{\partial t}\rho + (\rho u_j)_{,j} = 0 \tag{2}$$

$$\frac{\partial}{\partial t}(\rho u_i) + (\rho u_i u_j)_{,j} = -p_{,i} + \tau_{ij,j} + \frac{1}{Fr^2}\rho g_i \tag{3}$$

$$u_{j,j} = -\frac{1}{Re_0 Sc}(ln\rho)_{,jj} \tag{4}$$

The viscous stress is Newtonian with

$$\tau_{ij} = \frac{\rho}{Re_0}[u_{i,j} + u_{j,i} - \frac{2}{3}u_{k,k}\delta_{ij}] \tag{5}$$

and the mass diffusion Fickian, with constant diffusion coefficient, $\mathcal{D}$. Note that Eqs. (2)-(3) are the usual continuity and momentum transport equations for compressible flows. Equations (2)-(4) can be rigorously derived from the fully compressible Navier-Stokes equations by letting $P, T \to \infty$ such that $p/(\mathcal{R}T) \to constant$. The latter condition ensures that the microdensities of the two fluids are constant. If the densities of the two fluids are commensurate, then the mixture density is close to its average value and Eqns. (2)-(4) lead to the Boussinesq approximation (see Ref. [7] for the derivation).

In Eqns. 2-4, u_i is the velocity in direction i, ρ is the mixture density, and p is the pressure. The non-dimensional parameters in equations (2)-(4) are the computational Reynolds number, Re_0, Schmidt number, Sc, and Froude number, Fr:

$$Re_0 = L_0 U_0 / \nu_0, \quad Sc = \nu_0 / \mathcal{D}, \quad Fr^2 = U_0^2 / (g L_0) \tag{6}$$

with g, the magnitude of the gravitational acceleration, taken to be constant. Here g_i are the components of the unit vector in the direction of gravity, g $= (0, 0, -1)$. The independent variables are the time t and space variables, x_i. The kinematic viscosity, $\nu_0 = \mu/\rho$, and mass diffusion coefficient, $\mathcal{D}$, are assumed constant. Note that, in general, the dynamic viscosity, μ, is a weaker function of density; the assumption ν_0 constant ensures a uniform Sc throughout the flow. The reference density, ρ_0, is chosen such that the density of the light fluid is 1.0. The domain size in the horizontal direction is $L_0 = 2\pi$ and Δ_v/Δ_h=0.8, where Δ_v and Δ_h are the mesh sizes in the vertical and horizontal directions, respectively. In order to minimize the computational requirements, the simulations start with a small dimension in the vertical direction and the vertical mesh size is increased as the mixing layer width grows. The final sizes in the vertical direction at the time of printing are $L_v = 22.6$ (4608 grid points) for the $1024^2 \times N_z$ simulations and $L_v \approx 5.0$ (4032 grid points) for the $4096^2 \times N_z$ simulation. The Froude number is chosen such that the mesh Grashoff number, $Gr \equiv 2A g \Delta_h^3 / \nu_0^2 = 2A Re_0^2 / (Fr^2 N_h^3)$, where N_h is the number of grid points in one of the horizontal directions, is below 1 (a value of 0.88 was used in all simulations).

Equations (2)-(4) have periodic boundary conditions in the horizontal direction and slip wall conditions are applied in the direction of gravity.

All simulations presented here have been performed with the CFDNS code [11]. A brief description of the numerical method can be found in Ref. [3]. In order to ensure the accuracy of the numerical solution, extensive resolution studies have been performed.

The density is initialized to follow an error function profile in the vertical direction, which is consistent to the solution to the pure diffusion equation:

$$\rho = 0.5 \left(1 + Erf\left[Y_v z + \zeta(x, y)\right]\right)(\rho_2 - \rho_1) + \rho_1, \tag{7}$$

with the slope coefficient Y_v chosen such that 8 grid points lie across the initial mixing layer. Various spectra are used for the perturbation $\zeta(x, y)$, to test the influence of the initial conditions. For each A considered, a base case has been run with the initial perturbation spectrum shape being a top-hat centered around the most unstable mode of the linear problem. All base cases have $Sc = 1$ and $Re_0 = 500$. In order to examine the influence of the molecular transport properties, simulations with $Sc > 1$ and/or $Re_0 \neq 500$ have also been carried out.

3. Results

To test various hypotheses related to the RT layer growth and elucidate the long-standing discrepancy between the experimentally and numerically measured growth rates, explore the turbulence and mixing characteristics, and provide data for model development and testing, we have performed fully resolved, very high resolution simulations of Rayleigh-Taylor instability with the CFDNS code [11]. These simulations are the largest fully resolved simulations of the
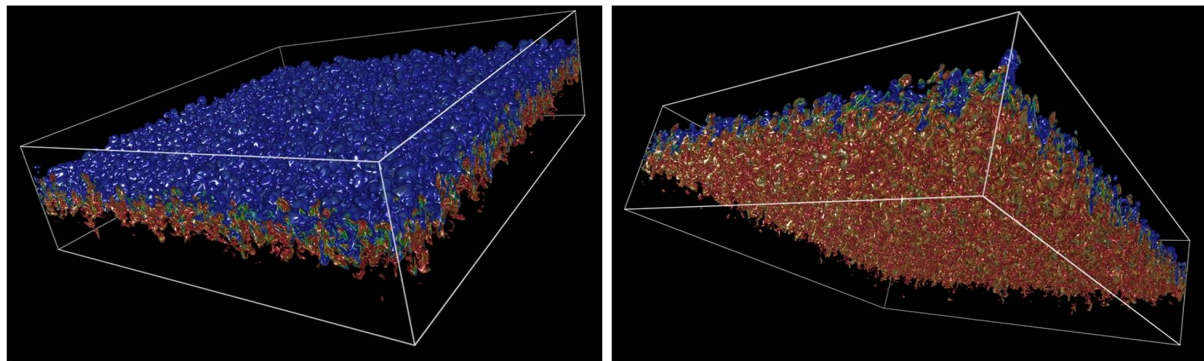
Figure 1. Three-dimensional visualization of the density field at early time, viewed from a) top and b) bottom, showing the asymmetry of the Rayleigh-Taylor mixing layer at $A = 0.75$, with the development of bubbles on the heavy fluid side and spikes on the light fluid side. From the $4096^2 \times 4032$ simulation.

Rayleigh-Taylor instability to date and cover the range of Atwood numbers, $A = 0.04 - 0.9$, in order to study small departures from the Boussinesq approximation as well as large Atwood number effects, which are even less understood (figure 1).

After the layer width had developed substantially, additional branched simulations have been run under reversed and zero gravity conditions (figure 2). This "gravity reversal" occurs in practical situations (e.g. ICF or pulsating stars), however there are no fully resolved simulations to date in this configuration.
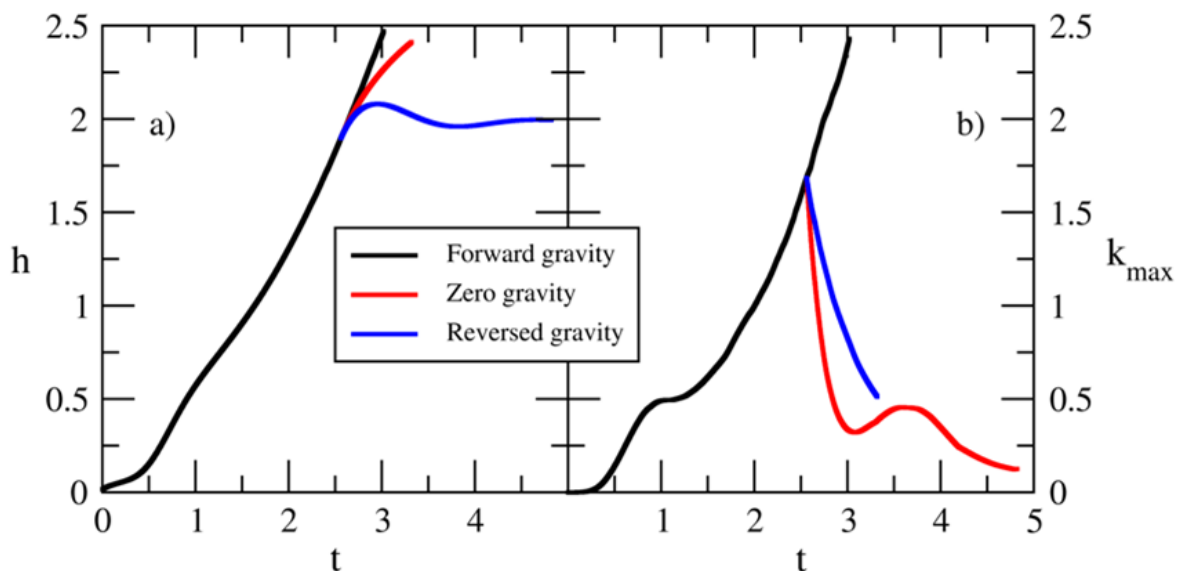

Figure 2. a) Layer width on the heavy fluid side (or "bubble height"), h_b, and b) maximum turbulent kinetic energy across the mixing layer from the base $A = 0.5$ simulation, on a $1024^2 \times 4608$ mesh. The main simulation (forward gravity) is branched into additional simulations with zero gravity and reversed gravity at time ≈ 2.5.

After the gravity changes, the layer still continues to grow for some time due to the inertia (figure 2). Nevertheless, the gravity reversal leads to significant small scale turbulence production

(figure 3). In general, the existent turbulence models do not capture well this process, so that the gravity reversal simulations represent an important test case for turbulence model development.
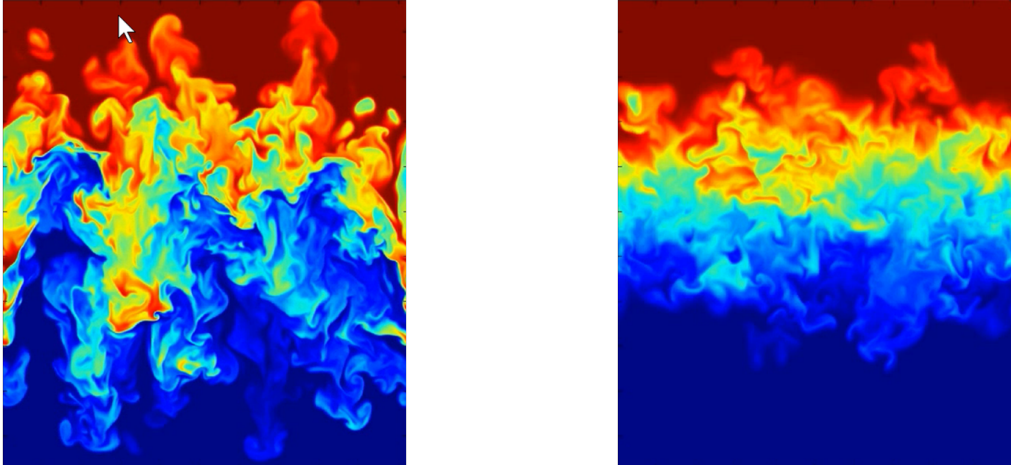

Figure 3. Snapshots of the density field from an $A = 0.5$ simulation. a) gravity, b) reversed gravity. The images are taken at the same time.

While the bulk of these results are still being analyzed and will be published elsewhere, here we present some preliminary results regarding the instability growth rate and mixing characteristics.

3.1. Mixing layer growth rates

The temporal evolution of the RT layer width is an important question in applications and one metric to gauge the efficacy of various models and numerical simulations. Although certain classes of initial conditions (e.g. if long wavelengths are present in the initial perturbation) may have a long lasting influence on the growth rate, it is generally agreed that at long times, if the turbulence growth is unrestricted, the turbulent mixing layer grows quadratically in time [12, 1, 2]:

$$h = \alpha A g t^2 + 2\sqrt{\alpha A g h_0}t + h_0 \tag{8}$$

The quadratic growth has been known for a long time as a dimensionally consistent result confirmed by experimental data [13, 14, 15, 16]. This formula, including various consistent ways for extracting the value of α, is further discussed in Ref. [3, 9]. Nevertheless, the value of the growth rate α is still hotly debated and there is a large discrepancy between the values reported by numerical simulations and many experiments, which constitutes a long-standing open question. To compound this open question, most numerical studies to date are under-resolved simulations relying on numerical errors to stabilize the Gibbs phenomenon. In addition, it is notoriously difficult, experimentally, to accurately characterize the initial conditions and provide the detailed measurements needed for turbulence model development and validation. The leading hypotheses for the discrepancy between the reported α values stem from these drawbacks– too large diffusion in the numerical simulations and undesired perturbations corrupting the initial conditions in the experiments. In our fully resolved simulations, we found little change in the value of α when varying the values of the molecular transport properties, if these are small enough. Small values for the molecular transport properties ensure small cut-off scales due to diffusion effects and, consequently, a large range of dynamically relevant scales of motion. We have also performed simulations with various initial perturbation spectra (figure 4).
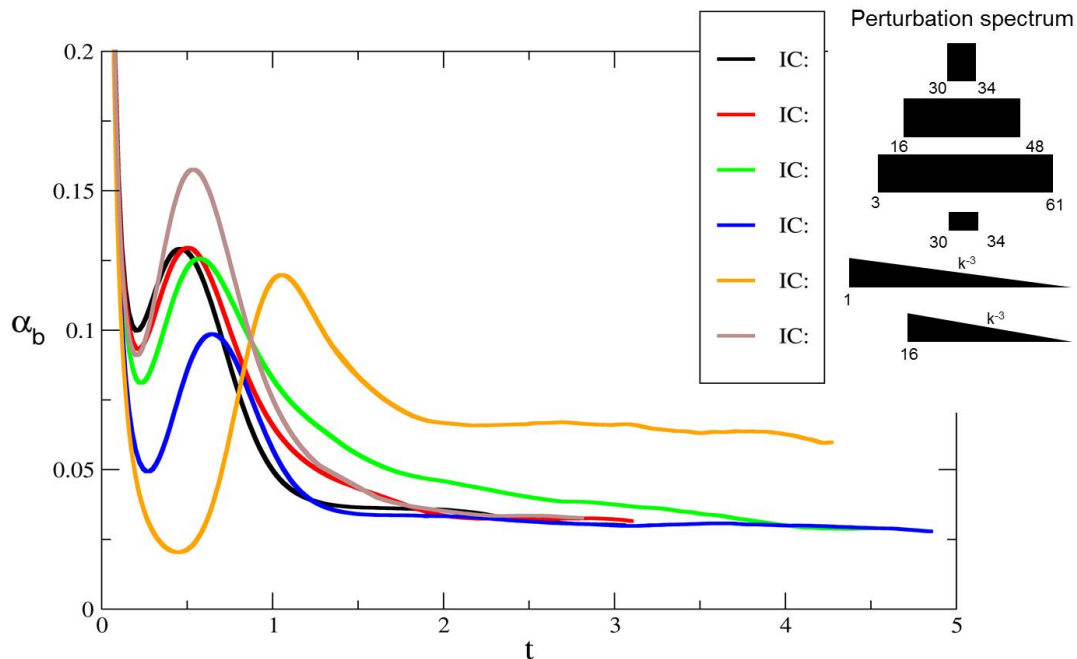
Figure 4. Rayleigh-Taylor bubble growth rate $\alpha_b = \frac{\cdot h_b^2}{4Agh_b}$ from several simulations with $A = 0.04$ and different initial perturbation spectra, shown in the legend. The light fluid side mixing layer growth rate has strong sensitivity to the Atwood number; the light fluid side growth rate is usually discussed in the previous studies.

The preliminary analysis of these results points to two possible explanations for the higher growth rates measured in various experiments (either one or both explanations can apply): 1) experimental set-up too small and thus the measurements represent only the early time behavior or 2) layer growth affected by the lateral walls due to large wavelengths present in the initial perturbation spectrum. To exemplify, figure 4 presents results from several simulations with top-hat initial perturbation spectra and different spectrum widths and/or amplitudes. Even though the early time behavior may suggest different growth rates, the long time results show the same asymptotic value for α. In a separate paper, we will survey the existent experimental studies and compare the experimental growth rates with the present results, using similar time non-dimensionalizations.

In addition, figure 4 also shows that simulations with specific perturbation spectra reproduce the higher α_b values seen in many experiments. Thus, when the simulation is initialized with a k^{-3} perturbation spectrum, values of $\alpha_b \approx 0.065$ are obtained. Similar α_b values are seen in all cases when a high amplitude, low wavenumber component is added to the initial perturbation (not shown here). While our results are preliminary, there are at least two experimental studies with carefully controlled initial conditions supporting the hypotheses above [17, 18]. Nevertheless, both of these hypotheses represent serious obstacles in characterizing the practical behavior, due to the lack of generality of the early time evolution and of the interaction with the walls. Using the present dataset, we will address the case of the instability development in a (laterally) confined domain as well as Atwood number effects on the instability growth, in a separate study.
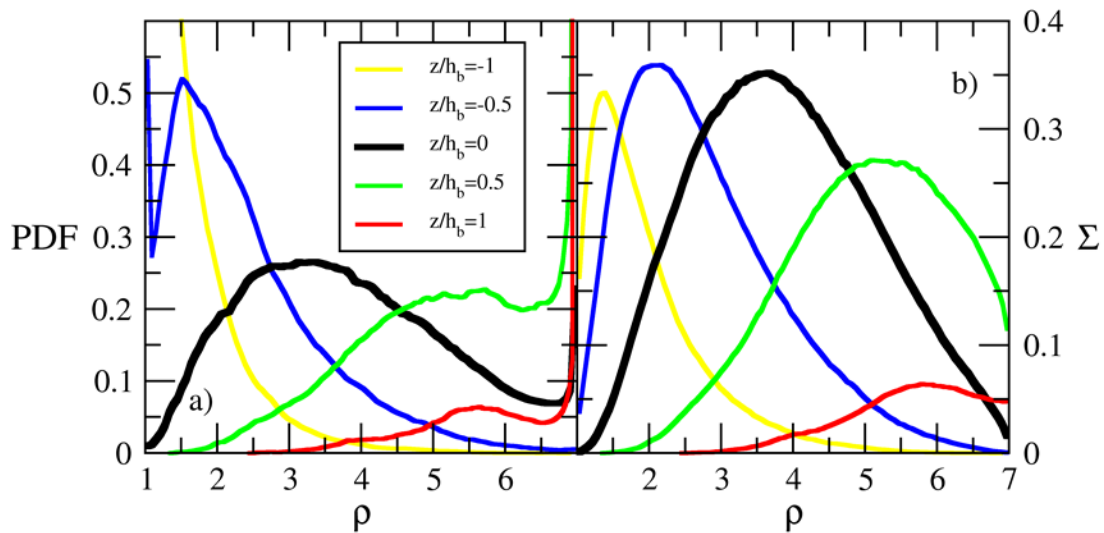
Figure 5. a) Density PDF and b) density surface density function Σ, at several positions across the mixing layer at $A = 0.75$, at the latest time of the $4096^2 \times 4032$ simulation. The vertical position is normalized by the bubble height, h_b.

3.2. Mix metrics and the mixing layer asymmetry

One of the more remarkable issues being explored with the new data set, first reported in Ref. [8] is the marked difference in the mixing between different density fluids as opposed to mixing that occurs between fluids of commensurate densities, corresponding to the Boussinesq approximation. Thus, at large density ratios, the mixing becomes asymmetric, with the pure heavy fluid mixing more slowly than the pure light fluid. The existence of this asymmetry is significant in practical applications. For example, it is important to know both how long it takes for a pollutant to mix with the surrounding fluid and also how much is likely left at a certain time. Predicting this based on Boussinesq analogies, as it is usually done, can severely misrepresent the mixing of the pollutant. One consequence of the mixing asymmetry for the Rayleigh-Taylor layer is that the penetration distance of the pure heavy fluid is larger than that of the pure light fluid [3]. Figure 5 a) shows the Probability Density Function (PDF) of the density at several locations across the mixing layer at $A = 0.75$. The density PDF varies considerably across the RT mixing layer. At the top of the RT layer the PDF is spiked at the heavy fluid end and includes some mixed fluid. At the bottom of the layer the PDF is spiked at the light fluid end. The PDF is clearly asymmetrical with respect to the centerline and the amount of pure heavy fluid reaching the centerline is larger than that of pure light fluid. At the edges of the layer, the consequence of the mixing asymmetry is even more obvious: the two edges develop into spikes on the light fluid side and bubbles on the heavy fluid side. This can be seen in figure 1, which shows the density field from the $4096^2 \times 4608$ simulation at $A = 0.75$. The asymmetry of the layer can also be inferred from figure 5 b), which shows the area of the $\rho^* = \rho$ iso-density surface, $\Sigma(\rho) = < |\nabla \rho^*|_{\rho^* = \rho} > PDF(\rho)$ [19], at several vertical locations across the mixing layer. On the light fluid side ($z/h_b < 0$), the dominant iso-surface has much larger surface area than on the heavy fluid side, indicating significantly more fragmentation.

In general, all mix metrics in use today for RT turbulence are constructed from lower order

moments of the density PDF. A comprehensive discussion of these metrics, including rigorous bounds, can be found in Ref. [8]. Thus, the usual mix measure $\theta = \frac{\langle f_1 f_2 \rangle}{F_1 F_2}$ [5] depends on the mean and variance of the density. Here $f_1 = \frac{\rho^* - \rho_1}{\rho_2 - \rho_1}$, $f_2 = \frac{\rho_2 - \rho^*}{\rho_2 - \rho_1}$ and $F_l = \langle f_l \rangle$, $l = \overline{1,2}$. While the density variance does appear in the dynamical equations in the Boussinesq limit [8], the moments equations at higher density ratios do not contain any term depending on $\langle \rho^2 \rangle$. From the point of view of the dynamical equations, a more appropriate mix metric at high A would be constructed from the density specific volume covariance, $\theta_{\rho v} = 1 - b/b_{nm}$ where $b = \langle \rho v \rangle$ and the no-mix value of b is $b_{nm} = \frac{(\bar{\rho} - \rho_1)(\rho_2 - \bar{\rho})}{\rho_1 \rho_2}$. Figure 5 shows that the two metrics are close at $A = 0.04$, as expected, but they are different at high A and differences increase with A. Thus, there is a qualitatively different behavior across the RT layer, as θ and $\theta_{\rho v}$ predict more mixing at the opposite sides of the layer. Nevertheless, both metrics have relatively large values across the whole layer, which misrepresents the density PDF. Nor they can capture any asymmetry in the underlying PDF. To compound the difficulty in characterizing the mixing state using low order moments of the density PDF, figures e) and f) show the same metrics across the mixing layer after the gravity was set to zero or reversed, at $A = 0.5$. The values are similar to those obtained for the base $A = 0.5$ case, although the mixing state is qualitatively different (figure 2). Other mix measures, e.g. using a fast reaction analogy, $\langle X_P \rangle$ [5], or the time-dependent Atwood number used in Ref. [20], while useful in certain instances, are still only low order representations of the underlying density PDF.

4. Summary and Concluding Remarks

We have presented preliminary results from high Reynolds number, high resolution Direct Numerical Simulations of Rayleigh-Taylor instability using the CFDNS code [11] on the 0.5 Petaflops, 150k compute cores BG/L Dawn supercomputer at Lawrence Livermore National Lab. This includes a suite of simulations with Atwood number ranging from 0.04 to 0.9 and grid size of $1024^2 \times 4608$ and a high resolution simulation of grid size $4096^2 \times 4032$ and Atwood number of 0.75. The reference cases have the initial perturbation spectrum as a narrow band around the most unstable mode of the linear problem. After the layer had developed substantially, the simulations have been branched, by reversing gravity and also setting the gravity to zero. In order to study the dependence on initial conditions, we have also performed a multitude of simulations with various initial perturbation spectra, different amplitudes of the initial perturbation, and also with several different values for the molecular viscosity and diffusivity.

While the bulk of the results are still being analyzed and will be published elsewhere, here we have presented preliminary results concerning two issues with significant practical importance: 1) the higher growth rates measured in experiments compared to previous numerical simulations and 2) mix metrics and mixing asymmetry.

Unlike most previous numerical simulations of RTI, which are under-resolved and rely on numerical errors to stabilize the Gibbs phenomenon, the present simulations fully resolve all the dynamically relevant scales of motion and use physical viscous and mass diffusion mechanisms. Thus, we can effectively vary the values of the molecular transport properties to assess their effects and the results show little dependence of the growth rate on these values, if they are small enough. Nevertheless, simulations with different spectra of the initial perturbation point to two hypotheses for the higher growth rates measured in various experiments (either one or both explanations can apply): a) experimental set-up too small and thus the measurements represent only the early time behavior or b) layer growth affected by the lateral walls due to large wavelengths present in the initial perturbation spectrum. While our results are preliminary, there are at least two experimental studies with carefully controlled initial conditions supporting the hypotheses above [17, 18]. Nevertheless, both of these hypotheses represent serious obstacles in characterizing the practical behavior, due to the lack of generality of the early time evolution
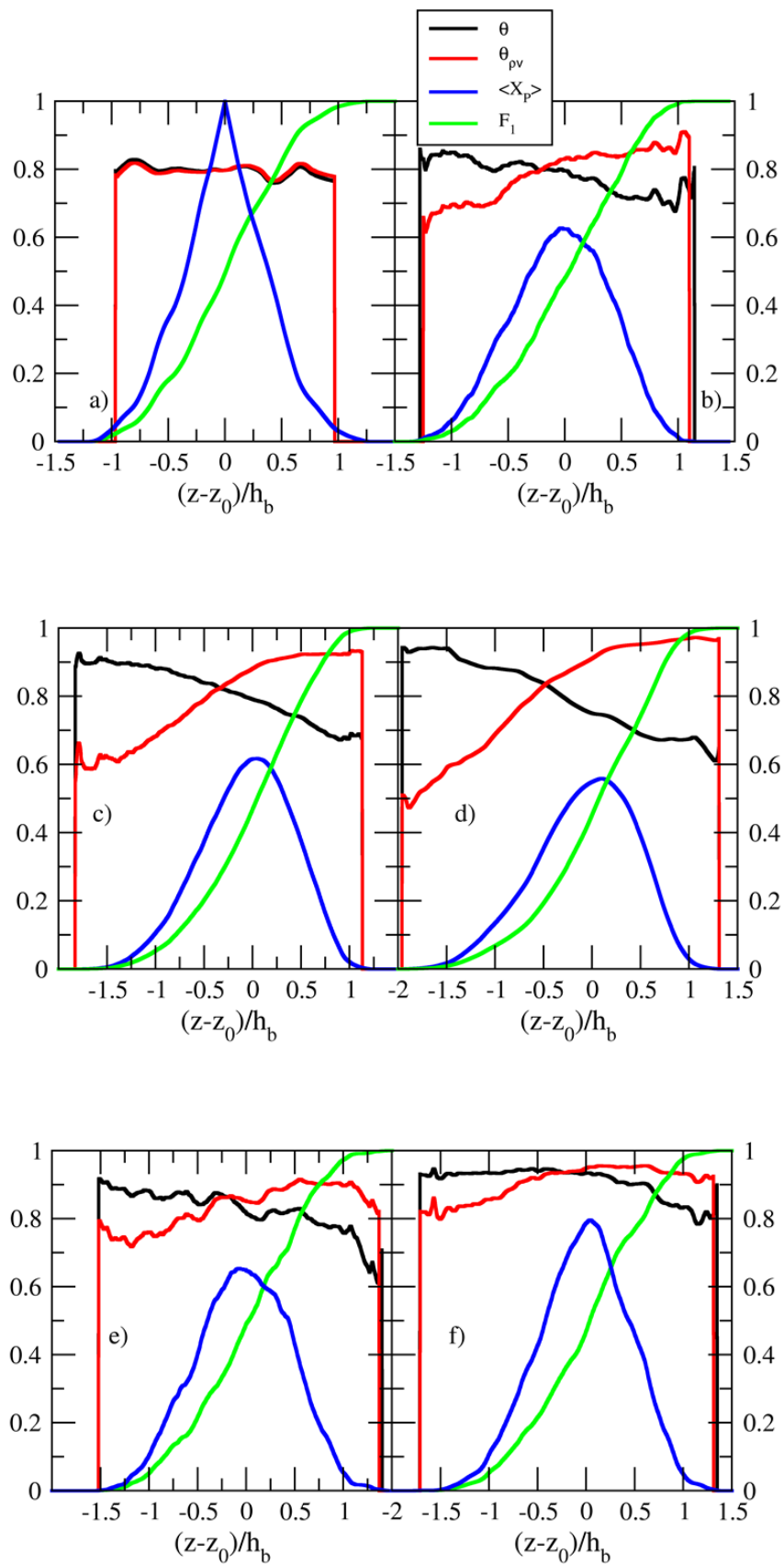
Figure 6. Several mix measures across the RT layer at a) $A = 0.04$, b) $A = 0.5$, c) $A = 0.75$, d) $A = 0.9$, e) $A = 0.5$, zero gravity, and f) $A = 0.5$, reversed gravity.

and of the interaction with the walls.

At high density ratios, the usual mix measure employed to characterize the mix state within the Rayleigh-Taylor mixing layer, θ, is no longer quasi-constant across the layer. Even more, the behavior is exactly the opposite as that obtained for a similar metric based on the density-specific volume correlation. This metric, $\theta_{\rho v}$, actually appears in the moment equations, so it would seem more appropriate at high A than θ. Nevertheless, none of these measures can tell much about the pure or partially mixed fluid or the underlying density PDF, which changes widely across the mixing layer.

Mixing is qualitatively different in VD flows compared to the Boussinesq limit, with the pure heavy fluid mixing more slowly than the pure light fluid [8]. This can be clearly seen in the density PDF and the density surface density function across the RT layer which are asymmetrical with respect to the centerline, showing that molecular mixing proceeds differently on the two sides of the RT layer. Experiments to date have not investigated this possibility. One consequence of the mixing asymmetry is that the penetration distance of the pure heavy fluid is larger than that of the pure light fluid. The mixing asymmetry is likely also related to the bubble-spike anomaly (higher growth rate on the spike side compared to the bubble side), which was observed experimentally.

4.1. Acknowledgments

5. References

[1] Cabot W and Cook A 2006 *Nature Phys.* **2** 562–568
[2] Livescu D, Ristorcelli J R, Gore R A, Dean S H, Cabot W H and Cook A W 2009 *J. Turbul.* **10** 1–32
[3] Livescu D, Ristorcelli J R, Petersen M R and Gore R A *Phys. Scr. T* **142** 014015–1–11
[4] Dimonte G and *et al* 2004 *Phys. Fluids* **16** 1668–1692
[5] Cook A W and Dimotakis P E 2001 *J. Fluid Mech.* **443** 69–99
[6] Cook A W, Cabot W H and Miller P L 2004 *J. Fluid Mech.* **511** 333–362
[7] Livescu D and Ristorcelli J R 2007 *J. Fluid Mech.* **591** 43–71
[8] Livescu D and Ristorcelli J R 2008 *J. Fluid Mech.* **605** 145–180
[9] Livescu D, Petersen M R and Wei T 2011 *to appear in Proceedings of the NECDC2010* (Los Alamos, NM)
[10] Chung D and Pullin D I 2010 *J. Fluid Mech.* **643** 279–308
[11] Livescu D, Mohd-Yusof J, Petersen M R and Grove J W 2009 CFDNS: A computer code for direct numerical simulation of turbulent flows Tech. rep. Los Alamos National Laboratory lA-CC-09-100
[12] Ristorcelli J and Clark T 2004 *LANL Report 03-4273 and J. Fluid Mech.* **507** 213–253
[13] Youngs D L 1984 *Physica D* **12** 32–44
[14] Read K I 1984 *Physica D* **12** 45–58
[15] Andrews M and Spalding D 1990 *Phys. Fluids* **A 2** 922–927
[16] Ramaprabhu P, Dimonte G and Andrews M J 2005 *J. Fluid Mech.* **536** 285–319
[17] Carles P, Huang Z B B, Carbone G and Rosenblatt C 2006 *Phys. Rev. Let.* **98** 104501 1–4
[18] Olson D H and Jacobs J W 2009 *Phys. Fluids* **21** 034103 1–13
[19] Vervisch L, Bidaux E, Bray K and Kollman W 1995 *Phys. Fluids* **7** 2496–2503
[20] George E and Glimm J 2005 *Phys. Fluids* **17** 054101–1–13